

# Complex differential variance algorithm for optical coherence tomography angiography

Ahhyun S. Nam,<sup>1,2,\*</sup> Isabel Chico-Calero,<sup>2,3</sup> and Benjamin J. Vakoc<sup>2,3,4</sup>

<sup>1</sup>Department of Mechanical Engineering, Massachusetts Institute of Technology, 77 Massachusetts Avenue, Cambridge, Massachusetts 02139, USA

<sup>2</sup>Wellman Center for Photomedicine, Massachusetts General Hospital, 50 Blossom Street, Boston, Massachusetts 02114, USA

<sup>3</sup>Harvard Medical School, 25 Shattuck Street, Boston, Massachusetts 02115, USA

<sup>4</sup>Department of Health Sciences and Technology, Harvard-MIT, Cambridge, Massachusetts 02139, USA  
\*snam@mit.edu

**Abstract:** We describe a complex differential variance (CDV) algorithm for optical coherence tomography based angiography. The algorithm exploits both the intensity and phase changes of optical coherence tomography (OCT) signals from flowing blood to achieve high vascular contrast, and also intrinsically reject undesirable phase signals originating from small displacement axial bulk tissue motion and instrument synchronization errors. We present this algorithm within a broader discussion of the properties of OCT signal dynamics. The performance of the algorithm is compared against two other existing algorithms using both phantom measurements and *in vivo* data. We show that the algorithm provides better contrast for a given number of measurements and equivalent spatial averaging.

©2014 Optical Society of America

**OCIS codes:** (170.4500) Optical coherence tomography; (170.3010) Image reconstruction techniques.

## References and links

1. T. Misgeld and M. Kerschensteiner, "In vivo imaging of the diseased nervous system," *Nat. Rev. Neurosci.* **7**(6), 449–463 (2006).
2. T. Schmoll, A. S. G. Singh, C. Blatter, S. Schriebl, C. Ahlers, U. Schmidt-Erfurth, and R. A. Leitgeb, "Imaging of the parafoveal capillary network and its integrity analysis using fractal dimension," *Biomed. Opt. Express* **2**(5), 1159–1168 (2011).
3. S. Makita, Y. Hong, M. Yamanari, T. Yatagai, and Y. Yasuno, "Optical coherence angiography," *Opt. Express* **14**(17), 7821–7840 (2006).
4. R. K. Wang, S. L. Jacques, Z. Ma, S. Hurst, S. R. Hanson, and A. Gruber, "Three dimensional optical angiography," *Opt. Express* **15**(7), 4083–4097 (2007).
5. A. A. Mariampillai, B. A. Standish, E. H. Moriyama, M. Khurana, N. R. Munce, M. K. K. Leung, J. Jiang, A. E. Cable, B. C. Wilson, I. A. Vitkin, and V. X. D. Yang, "Speckle variance detection of microvasculature using swept-source optical coherence tomography," *Opt. Lett.* **33**(13), 1530–1532 (2008).
6. S. H. Yun, G. J. Tearney, J. F. de Boer, N. Iftimia, and B. E. Bouma, "High-speed optical frequency-domain imaging," *Opt. Express* **11**(22), 2953–2963 (2003).
7. B. J. Vakoc, R. M. Lanning, J. A. Tyrrell, T. P. Padera, L. A. Bartlett, T. Stylianopoulos, L. L. Munn, G. J. Tearney, D. Fukumura, R. K. Jain, and B. E. Bouma, "Three-dimensional microscopy of the tumor microenvironment in vivo using optical frequency domain imaging," *Nat. Med.* **15**(10), 1219–1223 (2009).
8. B. Braaf, K. A. Vermeer, K. V. Vienola, and J. F. de Boer, "Angiography of the retina and the choroid with phase-resolved OCT using interval-optimized backstitched B-scans," *Opt. Express* **20**(18), 20516–20534 (2012).
9. L. An, J. Qin, and R. K. Wang, "Ultrahigh sensitive optical microangiography for in vivo imaging of microcirculations within human skin tissue beds," *Opt. Express* **18**(8), 8220–8228 (2010).
10. A. Szkulmowska, M. Szkulmowski, D. Sznajda, A. Kowalczyk, and M. Wojtkowski, "Three-dimensional quantitative imaging of retinal and choroidal blood flow velocity using joint Spectral and Time domain Optical Coherence Tomography," *Opt. Express* **17**(13), 10584–10598 (2009).
11. G. Liu, A. J. Lin, B. J. Tromberg, and Z. Chen, "A comparison of Doppler optical coherence tomography methods," *Biomed. Opt. Express* **3**(10), 2669–2680 (2012).
12. C. Blatter, J. Weingast, A. Alex, B. Grajciar, W. Wieser, W. Drexler, R. Huber, and R. A. Leitgeb, "In situ structural and microangiographic assessment of human skin lesions with high-speed OCT," *Biomed. Opt. Express* **3**(10), 2669–2680 (2012).

- Express **3**(10), 2636–2646 (2012).
13. B. J. Vakoc, S. H. Yun, J. F. de Boer, G. J. Tearney, and B. E. Bouma, “Phase-resolved optical frequency domain imaging,” *Opt. Express* **13**(14), 5483–5493 (2005).
  14. B. J. Vakoc, G. J. Tearney, and B. E. Bouma, “Statistical Properties of Phase-Decorrelation in Phase-Resolved Doppler Optical Coherence Tomography,” *IEEE Trans. Med. Imaging* **28**(6), 814–821 (2009).
  15. B. Braaf, K. A. Vermeer, V. A. D. P. Sicam, E. van Zeeburg, J. C. van Meurs, and J. F. de Boer, “Phase-stabilized optical frequency domain imaging at 1- $\mu\text{m}$  for the measurement of blood flow in the human choroid,” *Opt. Express* **19**(21), 20886–20903 (2011).
  16. J. Fingler, D. Schwartz, C. Yang, and S. E. Fraser, “Mobility and transverse flow visualization using phase variance contrast with spectral domain optical coherence tomography,” *Opt. Express* **15**(20), 12636–12653 (2007).
  17. G. Liu, L. Chou, W. Jia, W. Qi, B. Choi, and Z. Chen, “Intensity-based modified Doppler variance algorithm: application to phase instable and phase stable optical coherence tomography systems,” *Opt. Express* **19**(12), 11429–11440 (2011).
  18. R. Motaghianezam and S. E. Fraser, “Logarithmic intensity and speckle-based motion contrast methods for human retinal vasculature visualization using swept source optical coherence tomography,” *Biomed. Opt. Express* **3**(3), 503–521 (2012).
  19. Y. Zhao, Z. Chen, C. Saxer, Q. Shen, S. Xiang, J. F. de Boer, and J. S. Nelson, “Doppler standard deviation imaging for clinical monitoring of in vivo human skin blood flow,” *Opt. Lett.* **25**(18), 1358–1360 (2000).
  20. L. Yu and Z. Chen, “Doppler variance imaging for three-dimensional retina and choroid angiography,” *J. Biomed. Opt.* **15**(1), 016029 (2010).
  21. S. H. Yun, C. Boudoux, G. J. Tearney, and B. E. Bouma, “High-speed wavelength-swept semiconductor laser with a polygon-scanner-based wavelength filter,” *Opt. Lett.* **28**(20), 1981–1983 (2003).
  22. W. Y. Oh, S. H. Yun, G. J. Tearney, and B. E. Bouma, “115 kHz tuning repetition rate ultrahigh-speed wavelength-swept semiconductor laser,” *Opt. Lett.* **30**(23), 3159–3161 (2005).
  23. S. H. Yun, G. J. Tearney, J. F. de Boer, and B. E. Bouma, “Removing the depth-degeneracy in optical frequency domain imaging with frequency shifting,” *Opt. Express* **12**(20), 4822–4828 (2004).
- 

## 1. Introduction

Fluorescence-based microscopy techniques are mainstays of high-resolution angiographic imaging [1]. However, optical coherence tomography (OCT)-based approaches are rapidly gaining acceptance. Relative to fluorescence microscopy (confocal or multiphoton), OCT is able to image over larger fields and to deeper locations within tissue [2]. Unlike fluorescence microscopy, OCT discriminates between intravascular and extravascular spaces by detecting signal dynamics; the complex scattering signal from flowing blood is time-varying, while the scattering from tissues is substantially more time-stable. Because early OCT-based approaches for detecting and interpreting these dynamics were suboptimal, the resulting images featured poor contrast and slow imaging times relative to fluorescence microscopy. Advances in OCT instrumentation speed [3–6] (through Fourier-domain OCT), acquisition strategies [7–9] (through novel beam scanning), and signal processing algorithms have significantly improved OCT-based angiographic imaging [10–12].

In this work, we describe angiography based on complex differential variance (CDV) - a signal processing algorithm that achieves high intravascular to extravascular region contrast while also providing strong rejection of artifactual signals from bulk tissue motion or instrument instability. To describe the design and operation of this algorithm, we include a broader discussion of the origin of OCT signal dynamics and the optimal construction of angiographic algorithms. CDV angiography is benchmarked against other published algorithms using both phantom measurements and *in vivo* data, and is shown to provide better contrast for a given number of measurements. By adopting this algorithm into OCT-based angiographic systems, it may be possible to improve contrast for a given number of acquisitions, or to achieve a reduced number of acquisitions while maintaining a given contrast.

## 2. Properties of OCT signals from mobile scatterers

An OCT-based angiographic algorithm is designed to detect changes in the OCT signals, and further to discriminate between the changes induced by blood flow (signal) from those induced by other sources (noise/artifacts). The most common sources of noise/artifacts are

tissue bulk motion and instabilities in the instrumentation (most commonly associated with a lack of synchronization between the laser source and data acquisition in a swept-source OCT configuration) [13]. Table 1 summarizes the properties of time-varying OCT signals that result from these and other sources of noise, and also from flowing blood. We have sub-classified the flow into small displacement and large displacement regimes. Here, displacement refers to the magnitude of the spatial translation of the scatterers between measurements relative to the imaging resolution; small displacement implies a translation of significantly less than the OCT imaging resolution, while large displacement implies a translation greater than the OCT resolution. In this work, bulk motion is limited to small displacements regimes. Large displacement bulk motion is often present in some *in vivo* imaging setups, but there remains a large set of applications where bulk motion can be constrained to small displacement regime by mechanical stabilization. Finally, unsynchronized source/DAQ (for swept-source OCT systems) and source A-line to A-line amplitude noise are included. Table 1 describes the properties of the OCT signal amplitude and phase changes resulting from each source of signal variation. We specifically highlight the statistical nature of the signal (deterministic or stochastic) and the degree of correlation of the signal across depth (if any). As we will show, the degree of depth correlation is important because it is possible to design algorithms that respond differently to depth-correlated and depth-uncorrelated signals, and to use this feature to thereby differentiate between signal variations according to their sources.

**Table 1. Characteristics of OCT signal changes from varying sources.**

Source of OCT signal variation		Changes in real amplitude $A(z,t + \Delta t) - A(z,t)$	Changes in phase $\phi(z,t + \Delta t) - \phi(z,t)^*$
Flow (small displacement)	Transverse	negligible	negligible
	Axial	negligible	<b>deterministic; correlated across vessel</b>
Flow (large displacement)	Transverse	<b>stochastic; uncorrelated across depth</b>	<b>stochastic; uncorrelated across depth</b>
	Axial	<b>stochastic; uncorrelated across depth</b>	<b>stochastic; uncorrelated across depth</b>
Bulk motion (small displacement)	Transverse	negligible	negligible
	Axial	negligible	deterministic; correlated across sample
Source/DAQ synchronization		negligible	deterministic; linearly dependent on depth
Source amplitude noise		stochastic; correlated across depth	negligible

\* We note that phase changes (in radians) can be large due to any source of modulation if the signal amplitude ( $A$ ) is very low relative to its expected (ensemble average) value, i.e., at speckle nulls. In this table, we describe phase changes under the assumption that the signal amplitude is on the order of the expected value.

The first four rows of Table 1 describe the OCT signal properties associated with blood flow and each is additionally illustrated in Fig. 1. The signals were generated using a model of OCT signal evolution from translating scatterers [14]. Complex signals were generated for both axial flow [Fig. 1(a)] and transverse flow [Fig. 1(b)], and the amplitude and phase of these signals are presented at three adjacent depth locations. Because these signals are presented as a function of time, they describe both small and large displacement flow; for small displacement flow measurements are acquired from time-points closely spaced on the x-axis, and for large displacement flow measurements are acquired from more widely separated time-points. We note that, regardless of the flow velocity, it is always possible to obtain a large-displacement flow signal by increasing the time separation between

measurements. Many angiographic algorithms operate with substantial time separations to move the resulting signals into this large displacement regime. For transverse flow at small displacements, the complex signal variations are negligible. For axial flow at small displacements, a deterministic phase shift is induced (Doppler phase shift manifesting as a linear phase gain) that is correlated across depth (note the similar linear trend across the three depth points in Fig. 1(b)). For transverse flow within the large displacement regimes, variations in both the amplitude and phase are induced and the variation measured between any two time points is stochastic and uncorrelated across depth. For large displacement axial flow, similar stochastic and depth-uncorrelated amplitude and phase changes are induced.

The lower half of Table 1 describes the time-varying properties of the signals that cause artifacts. For small displacement bulk motion, only axial motion induces a significant signal change, and this is a depth-correlated and deterministic phase shift (i.e. the conventional Doppler shift). The presence of unsynchronized data acquisition and laser sweeping induces a similar deterministic and depth-correlated phase signal. Finally, source A-line repeatability noise induces a stochastic amplitude noise but has no significant effect on phase. This amplitude noise is practically negligible with most applications.

From Table 1, it can be appreciated that phase-based approaches require additional phase stabilization [13,15] or phase noise estimation and compensation [3,16] since they are susceptible to artifacts from bulk motion (small displacement) and unsynchronized laser/DAQ modules. For this reason, many recent approaches use only the OCT signal amplitude, and employ large time separations to operate in the large displacement regime [5,12,17,18]. As shown in Table 1, flow in this large displacement regime induces changes in both amplitude and phase, and these changes are stochastic in nature. In this work, we will show that it is advantageous to detect both the amplitude and phase components of the signal to more accurately identify flow-based changes. We will introduce the CDV algorithm that detects these amplitude and phase variations associated with flow but rejects the depth correlated phase changes induced by small displacement axial bulk motion and source/DAQ unsynchronized operation. Specifically, the CDV algorithm benefits from the detection of the additional phase dimension but avoids the necessity for phase compensation.

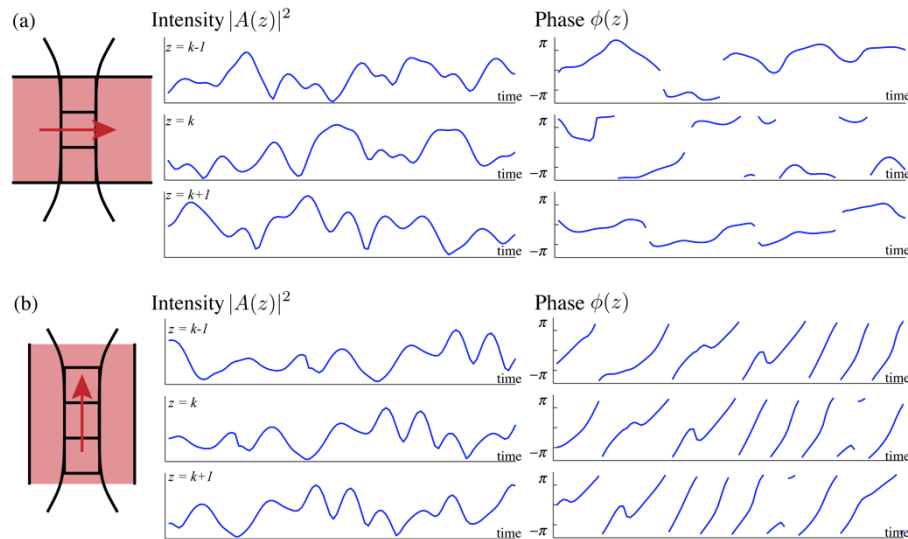


Fig. 1. Time characteristic of OCT signals from (a) transverse and (b) axial flows presented at three depth locations as a function of time.

### 3. OCT angiography based on complex differential variance (CDV)

In the following description of the CDV algorithm, each A-line is denoted by an array of complex signals  $R(z,t)$  where  $z$  and  $t$  are integer indices to discrete depth and time samples. It is assumed that the signals within an angiographic calculation were obtained at the same transverse location and therefore transverse indexing is not included for readability. Where appropriate, the complex signal will be expressed as  $R(z,t) = A(z,t)e^{i\phi(z,t)}$  where the amplitude  $A(z,t)$  is real. We assume a set of  $M$  measurements at each location providing time indexing from 1 to  $M$ , and depth indexing from 1 to  $N_z$ .

The complex differential variance algorithm applied to a single pair of A-lines at time indices  $t = 1$  and  $t = 2$  is given by

$$f_{CDV}(z) = \sqrt{1 - \frac{\left| \sum_{k=-L}^L w(k) R(z-k,1) R^*(z-k,2) \right|}{\sum_{k=-L}^L w(k) \frac{1}{2} \left[ |R(z-k,1)|^2 + |R(z-k,2)|^2 \right]}}, \quad (1)$$

where  $w(k)$  is a depth window function of length  $2L + 1$ . The algorithm calculates the ratio of the magnitude of a complex correlation term between two time points summed across a depth kernel defined by  $w(k)$  to a similar summation of magnitudes. We note that the numerator is similar to an autocorrelation expression of delay  $\Delta t = 1$  (across time) except summation is performed in the depth dimension. We note that the CDV algorithm is sensitive to any changes in amplitude. Additionally, the CDV algorithm is sensitive to changes in phase only when they are varying across the depth window defined by  $w(z)$ . Therefore, both the amplitude and phase stochastic variations from flow contribute to the angiographic signal but small amplitude bulk motion and unsynchronized laser/DAQ modules have negligible contributions.

A visual illustration of how the CDV algorithm operates on large displacement flow and small displacement axial bulk motion is presented in Fig. 2. For simplicity, the CDV vascular contrast is calculated for the middle voxel from two sequential measurements with a rectangular window  $w(z)$  of length 5. The arrowed vectors represent complex OCT data  $R(z,t)$  in the complex plane. Figure 2(a) describes how CDV suppresses the phase noise from a static region subject to a small displacement bulk motion and other phase noise. The time changes are calculated from the conjugate multiplication of the A-line pair as a complex differential and represented by the blue vectors in the figure. The fractional term in Eq. (1) comes from two summations on the complex plane. The numerator is the magnitude of the vector sum of the blue vectors in the complex differential A-line. The denominator is computed by the summation of the red vectors, which are the arithmetic average of the intensities. Since the magnitude does not change over time and the differential phase is constant over depth, the numerator and denominator are equal. Thus the constant phase noise is virtually removed and the signal is nearly zero. Note that the depth directional summation is essentially a calculation of directional variance of the complex differential vectors. Figure 2(b) describes the contrast calculation in the flow region where both the amplitude and phase change over time. Since the complex differential vectors are at random, the numerator term is always smaller than the denominator and a nonzero contrast value is obtained.

The application of the CDV algorithm to more than 2 measurements is optimally performed as

$$f_{CDV}(z) = \sqrt{1 - \frac{\sum_{t=1}^{M-1} \left| \sum_{k=-L}^L w(k) R(z-k, t) R^*(z-k, t+1) \right|}{\sum_{t=1}^{M-1} \sum_{k=-L}^L w(k) \frac{1}{2} \left[ |R(z-k, t)|^2 + |R(z-k, t+1)|^2 \right]}}, \quad (2)$$

where the summation across measurements is performed within the numerator and denominator after the depth summation but before division.

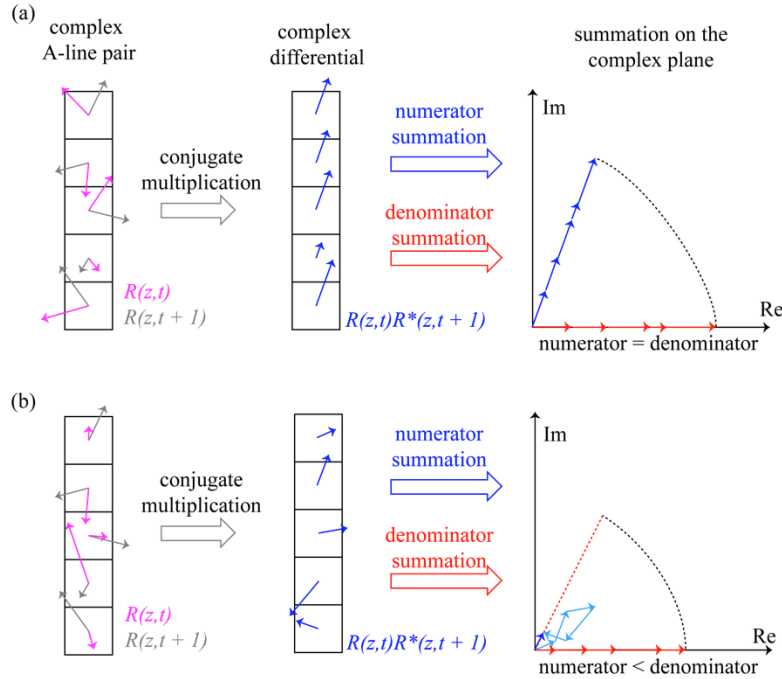


Fig. 2. Illustration of the CDV algorithm for static and flow voxels. In the first column, the complex signal as a function of depth is illustrated for a first (purple) and second (grey) measurement. In the second column, the complex cross correlation between these measurements are presented. In (a), a static region undergoing bulk axial motion (or a static region acquired with DAQ synchronization errors) is presented. In (b), a flow region (large displacement, axial or transverse) is presented. In (a), the correlated phase shifts across depth do not significantly alter the summed vector length in the numerator (blue) relative to the denominator (red). In (b), the numerator sums to a smaller magnitude vector relative to the denominator due to uncorrelated phase signals across depth and variations in signal amplitude across time.

To demonstrate immunity to bulk motion and source/DAQ synchronization failures, we acquired OCT signals from human skin and compare processed angiograms using the CDV and phase resolved Doppler variance [19,20], another angiographic algorithm that incorporates both phase and amplitude data. Two algorithms differ in their nature of treating multiple measurements. While phase resolved Doppler variance computes the temporal variance of all measurements CDV takes a pairwise differential and the variance within the specified depth-kernel, and later performs time averaging. As described previously, the differential processing is essential for the inherent immunity to the depth-correlated phase noise. Figure 3 compares the cross-sectional vascular contrast images generated from data acquired with an OCT system described in Section 4 with 7 measurements per each transverse location with a time delay of 6 ms. The phase noise due to phase instability and/or bulk

motion manifests as the characteristic vertical banding [Fig. 3(c)]. This is absent in the vascular tomogram generated from CDV [Fig. 3(b)].

We note that depth summation in CDV includes blurring along the depth axis over an extent defined by the width of the kernel  $w(z)$ . The impact of this blurring is relatively small in OCT-based angiography for several reasons. First, due to shadow artifacts, OCT images are intrinsically distorted along the axial dimension. Therefore, it is appropriate to apply averaging first to the depth dimension before the transverse dimensions, which are not affected by shadowing. Second, the extent of the blurring is small. We have explored angiographic performance as a function of the width of  $w(z)$ , and found that optimal imaging is achieved for kernels of limited widths (full width half max of 24  $\mu\text{m}$  in air). Third, most angiographic images are displayed and analyzed in *en face* presentations where axial blurring is hidden within the out-of-plane direction.

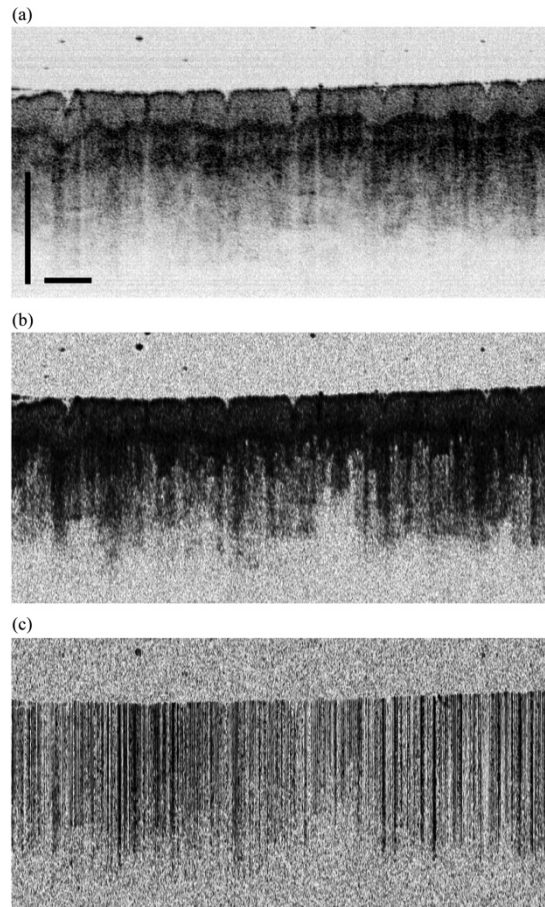


Fig. 3. Cross-sectional OCT images of human skin. (a) Structural image. (b) Vascular contrast computed from CDV. (c) Vascular contrast computed from phase resolved Doppler Variance. The motion and DAQ synchronization artifacts show as vertical bands in (c). Both algorithms use phase data in angiographic processing but the CDV is insensitive to the depth-correlated phase signals induced by bulk motion and DAQ synchronization errors. Scale bars = 1 mm.

#### 4. Benchmarking methodology and experimental setup

To evaluate the performance of the CDV algorithm, we compare its performance to a subset of published algorithms using data acquired with an optical frequency domain imaging (OFDI) system. The OFDI system is similar to that used in previous studies [7,13]. A

wavelength swept laser source [21] with an end reflector [22] centered at  $\lambda_c = 1285$  nm with a bandwidth  $\Delta\lambda = 140$  nm was operated at a 50 kHz A-line rate with 20 mW average power. The system employs a fiber-optic based interferometer with a 25MHz acousto-optic frequency shifter in the reference arm to avoid depth degeneracy of the image [23]. A dual balanced receiver is used to detect the signal. In the microscope interface, a commercial OCT scan-lens (Thorlabs LSM02) is used after a galvanometer beam scanner (Cambridge technology 6757). The configuration results in a transverse resolution of  $\sim 20$   $\mu\text{m}$  and a maximum lateral scan range of 12 mm in each direction, where 1184 A-lines are acquired per frame. The complex OCT A-line data is generated with the standard OFDI processing method [23] for further angiographic processing.

**Table 2. Summary of OCT based angiography algorithms**

Algorithm	Contrast formula
Power intensity differential (PID) [12]*	$f_{PID}(z) = \sum_{t=1}^{M-1} [I(z, t+1) - I(z, t)]^2$ <p>where <math>I(z, t) = 20 \log_{10} R(z, t)</math></p>
Intensity-based Doppler variance [17]*	$f_{IBDV}(z) = 1 - \frac{\sum_{t=1}^{M-1} \sum_{k=-L}^L w(k)  R(z-k, t)   R(z-k, t+1) }{\sum_{t=1}^{M-1} \sum_{k=-L}^L w(k) \frac{1}{2} [  R(z-k, t) ^2 +  R(z-k, t+1) ^2 ]}$
Complex differential variance	$f_{CDV}(z) = \sqrt{1 - \frac{\sum_{t=1}^{M-1} \sum_{k=-L}^L w(k) R(z-k, t) R^*(z-k, t+1)}{\sum_{t=1}^{M-1} \sum_{k=-L}^L w(k) \frac{1}{2} [  R(z-k, t) ^2 +  R(z-k, t+1) ^2 ]}}$

\* The contrast formulae are presented in their original form without square-root transformation

To quantify algorithm performance, a two-region phantom was constructed to simulate static and mobile scatterers. The static scattering was simulated by a piece of Teflon, and the mobile scatterers were simulated by 0.5% intralipid solution. Variations in the optical scattering signal from intralipid resulted from Brownian motion, but in the large time separation regime these signal decorrelations are statistically similar to those resulting from translational flow. To approximately match signal SNR, the intralipid concentration was selected to provide similar signal strength as that of Teflon near the surface. To compare algorithm performance *in vivo*, data was obtained from a mouse dorsal skinfold chamber.

The CDV was benchmarked against a subset of published amplitude-based angiographic algorithms [5,12,17,18] that offer a similar rejection of artifactual signals from small displacement bulk motion and an unsynchronized source/DAQ. To avoid ambiguity, we present the exact angiographic expression used for each algorithm in Table 2. Included are: an algorithm providing vascular contrast through calculation of the power intensity differential (PID) of log-scale intensity [12,18] and an evolution of the phase resolved Doppler variance method (highlighted previously in Section 3) termed intensity-based Doppler variance (IBDV) [17]. Of note, among these two algorithms and CDV, only CDV includes phase data in the angiographic calculation. In benchmarking these algorithms, we used only two time points (a single pair) and each algorithm operated on exactly the same data. The time difference between these measurements for all acquired data is 12 ms. Each of PID and IBDV was modified as shown in Table 2 to incorporate depth averaging across a kernel of 24  $\mu\text{m}$  FWHM in air (Hann window), equivalent to that used for CDV. We also note that each vascular data was modified with a square root transformation to better match the histogram distribution to CDV. This square-root transformation affects the appearance of the images but does not affect the quantitative contrast metrics used to evaluate the algorithms.

## 5. Angiographic algorithm performance comparison

The angiogram images of the phantom [Figs. 4(a) and 4(b)] for each algorithm are displayed as 8-bit images using the MATLAB Jet colormap [Figs. 4(c), 4(e) and 4(g)] where regions of interest (ROIs) for the static and mobile areas are defined by the rectangular boxes of white dashed line and black solid line, respectively. For easier interpretation and fair comparison, each image was displayed using a linear transformation with scaling and offset parameters that mapped the average static angiographic signal within the first ROI to 0.3, the average mobile static angiographic signal within the second ROI to 0.6, and with a colormap spanning the range from 0 to 1.2. In these displays, respective ROI box therefore has the same average color, but has differing variability in color. In Figs. 4(d), 4(f) and 4(h), we present the histograms for each ROIs. Here, the histograms from the IBDV and PID algorithms are scaled such that the average mobile signal matches that of the unscaled CDV algorithm (i.e., that provided directly by Eq. (1)), but zero-values are retained for each algorithm (i.e., a zero form each algorithm maps to zero on the x-axis).

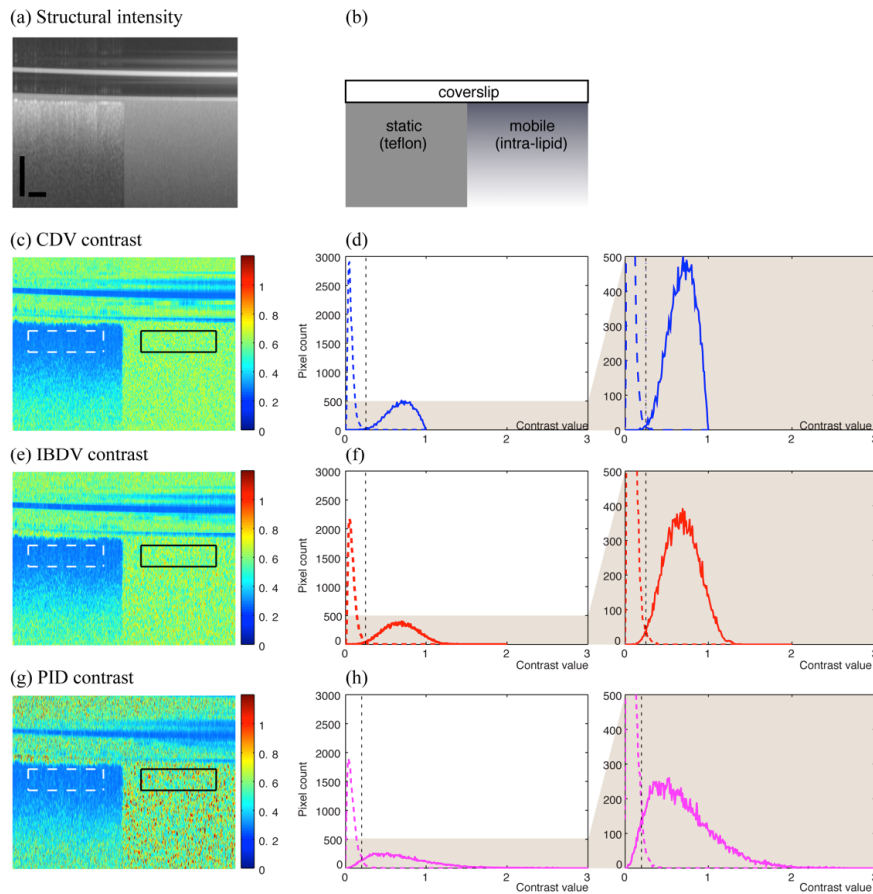


Fig. 4. Phantom analysis: (a) a structural image and (b) a schematic of the phantom. (c, e, and g) contrast images with marked ROIs and (d, f, and h) the histograms of CDV, IBDV, and PID algorithms, respectively. The static ROI data is marked with a dashed line and the mobile ROI data with a solid line. Scale bars = 1 mm.

We note that across the three algorithms, the histograms of mobile scatterers show marked variations in distribution shape whereas the histograms from static scatterers are more similar. PID results in the longest high-side tail on the mobile scatterers. CDV has the most

concentrated distribution of signals from mobile scatterers. This reduced variation of signals from mobile scatterers is attributed to the inclusion of additional phase dimension as described in Section 3. For static distributions, CDV and IBDV show smaller standard deviations compared to PID. This can be explained by PID's use of logarithmic intensity that amplifies variance at speckle nulls. The effect of speckle nulls is additionally mitigated in CDV and IBDV due to the weighted averaging prior to division (i.e., independently averaging in the numerator and denominator).

To quantify the separation of the histograms presented in Figs. 4(d), 4(f) and 4(h), we computed the two-state classification error rate. We first calculated the signal threshold for each algorithm that results in equivalent rates of static pixels falling above the threshold as mobile pixels falling below the threshold. The misclassification rate using this threshold is then provided as the overall classification error rate with other statistical measurements in Table 3. The classification error rate for CDV is approximately 4.7 fold smaller than IBDV and 25.9 fold smaller than PID.

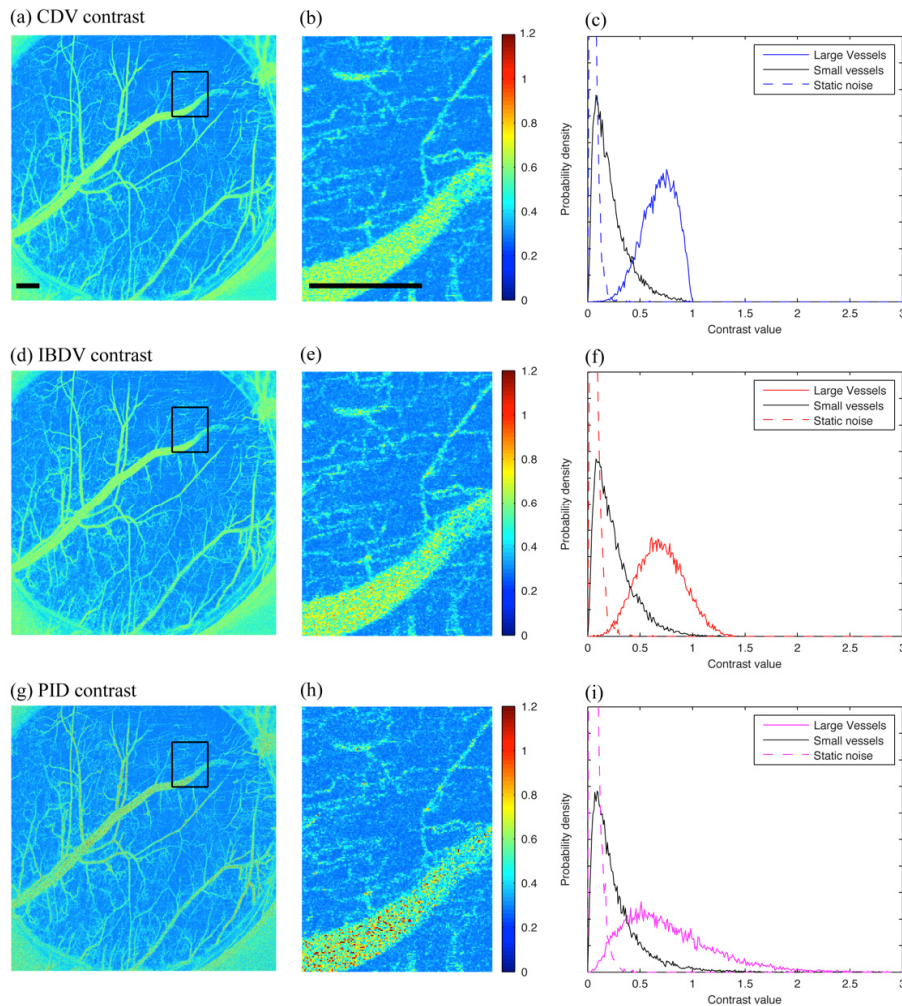


Fig. 5. *In vivo* contrast comparison: (a, d, and g) single full-field *en face* plane vascular contrast images of a mouse dorsal skinfold chamber and the magnified view (b, e, and h) of the ROI - marked with black rectangles, and (c, f, and i) the histograms of manually segmented regions. Scale bars = 1 mm.

In Fig. 5, the algorithm performance is compared on *in vivo* data acquired from a mouse dorsal skinfold chamber. The angiographic images in Figs. 5(a), 5(d) and 5(g) are of a single *en face* plane of the volume data and are presented with the same mapping as used in Figs. 4(c), 4(e), and 4(g). The ROIs marked in Figs. 5(a), 5(d) and 5(g) are magnified in Figs. 5(b), 5(e) and 5(h). To quantitatively analyze the signals, we generated a set of ROIs describing large vessel intravascular regions, capillary intravascular regions, and extravascular regions. Multiple smaller ROIs for each region were defined and combined to describe each region globally. To avoid bias, we identified these smaller ROIs angiograms created by each of the algorithms. The capillary regions were defined by locating the centerline of a capillary, and using the space within 1 pixel of this centerline.

We analyzed signal histograms in each of these three regions and display these in Figs. 5(c), 5(f) and 5(i) using the same scaling as in Figs. 4(c), 4(f) and 4(i). The performance trends described in the phantom experiments are recapitulated in the *in vivo* data. Large vessels in CDV have the most concentrated distribution skewed away from the static distribution. For the noise floor, CDV and IBDV show smaller standard deviation compared to PID. Signals within the capillaries were not well matched to either the mobile statistics or the static statistics. This is likely due to a combination of these voxels containing both static and mobile scatterers. Further algorithm development work could focus on optimizing contrast in these critical vessels.

**Table 3. Algorithm performance metrics for phantom analysis**

	CDV	IBDV	PID
<b>Classification error rate [%]</b>	0.175	0.820	4.54
<b>Threshold value</b>	0.253	0.251	0.200
<b>Mobile mean*</b>		0.690	
<b>Mobile standard deviation</b>	0.154	0.205	0.375
<b>Static mean</b>	0.0710	0.0867	0.0841
<b>Static standard deviation</b>	0.0362	0.0468	0.0555

\* The histograms are scaled to have the same mobile mean with the CDV contrast for easier interpretation.

## 6. Conclusion

We have presented the CDV algorithm for OCT-based angiography that achieves high vascular contrast by detecting modulations in both signal amplitude and signal phase but intrinsically rejects the effect of phase modulations due to bulk motion and data acquisition synchronization errors. The performance of the CDV algorithm is compared with other intensity based algorithms that are immune to the phase noise. In the phantom histogram analysis, it is shown that CDV provides better contrast in phantom histogram analysis, where the contrast performance was quantified by the classification error rate. CDV also showed the most concentrated distribution of signals in the flow region for the given number of acquisitions. This trend is repeated in the *in vivo* vascular images. Improved angiographic signal processing algorithms can be used to either improve image contrast without increasing imaging time, or to accelerate imaging times without sacrificing contrast.

## Acknowledgments

This project was supported by the Center for Biomedical OCT Research and Translation through Grant Number P41EB015903, awarded by the National Center for Research Resources and the National Institute of Biomedical Imaging and Bioengineering of the National Institutes of Health. This work was also supported by NIH grant R01CA163528. Ahhyun S. Nam was partially supported by Graduate Student Fellowship of Wellman Center for Photomedicine and Kwanjeong Educational Foundation.